buildings

MDPI

Article

Evaluation of Rotation Capacity and Bauschinger Effect Coefficient of I-Shaped Beams Considering Loading Protocol Influences

Yoshihiro Kimura

Graduate School of Engineering, Tohoku University, Sendai 980-8579, Japan; kimura@tohoku.ac.jp; Tel.: +81-22-795-7865

Abstract: Recent catastrophic earthquake events have reinforced the necessity of evaluating the seismic performance of buildings. Notably, the buildings can go into the plastic phase during a striking earthquake disaster. Under this condition, the current design codes assume seismic response reduction by virtue of the energy dissipation capacity of the structural members. In the strong-column–weak-beam design, which involves I-shaped beams and boxed columns, the mechanism is defined as a standard design scheme to prevent the building from collapsing. Therefore, energy dissipation relies highly on the I-shaped beam performance. However, the I-shaped beam performance can differ depending on the loading history experienced, whereas this effect is untouched in the prevailing evaluation equation. Hence, this study first performs cyclic loading tests of 11 specimens using different loading protocols. The experimental results clarify the fluctuation in the structural performance of I-shaped beams depending on the applied loading hysteresis, proving the necessity of considering the stress history for proper assessment. Furthermore, the database of experimental results is constructed based on the previous experimental studies. Ultimately, the novel evaluation equation is proposed to reflect the influences of the loading protocol. This equation is demonstrated to effectively assess the member performance retrieved from the experiment of 65 specimens, comprising 11 specimens from this investigation and 54 specimens from the database. The width–thickness ratio, shear span-to-depth ratio, and loading protocols are utilized as the evaluation parameters. Moreover, the prediction equation of the Bauschinger effect coefficient is newly established to convert the energy dissipation capacity under monotonically applied force into hysteretic energy dissipation under the cyclic forces.

Keywords: I-beam; rotation capacity; energy dissipation capacity; Bauschinger effect coefficient; loading protocol

Citation: Kimura, Y. Evaluation of Rotation Capacity and Bauschinger Effect Coefficient of I-Shaped Beams Considering Loading Protocol Influences. *Buildings* **2024**, *14*, 1376. https://doi.org/10.3390/buildings14051376

Academic Editor: Hugo Rodrigues

Received: 28 March 2024
Revised: 30 April 2024
Accepted: 9 May 2024
Published: 11 May 2024

1. Introduction

I-shaped steel beams (I-beams) are widely utilized in steel moment-resisting frames (MRFs) due to their high in-plane bending stiffness and strength against applied bending moments. However, in addition to dead and live loads, seismic loads increase the bending moment, leading to instability phenomena such as lateral buckling and local buckling. The research on I-beams initiated by elucidating these buckling phenomena through classical theory [1,2] and then expanded to evaluate lateral buckling resistance and rotation capacity [3–25]. Since main girders in frames are typically connected to restraining beams or concrete slabs, studies on buckling stiffening and stress transfer mechanisms between these components [26–33] have improved the performance evaluation of beams in frames. Additionally, numerous analytical and experimental studies have assessed the width–thickness ratio, ultimate bending strength, and rotation capacity to avoid plate buckling of the flange and web. Through these efforts, the beam can exhibit sufficient plastic rotation during a major earthquake by limiting the width-to-thickness ratio [34–52]. Regarding the width–thickness ratio, the prevailing design codes [53,54] specify their values for the

member classifications. Even though recent provisions by AIJ [55] included the index with the web–flange interactions, the loading protocol influence was not reflected in the evaluation equation.

The mechanical performance of I-beams has been extensively studied in previous experimental research, such as the work by Kato et al. and Lignos, D. G. et al. [56–61]. Furthermore, the loading protocol and slenderness ratio influences are addressed in previous studies [62,63], whereas the evaluation scheme has not been established in an explicit manner. The evaluation criteria typically involve the rotation capacity for unidirectional loading (monotonic loading) and the energy dissipation capacity for cyclic loading. Parameters such as the width–thickness ratio of the member, shear span-to-depth ratio, or loading conditions are considered. The energy dissipation capacity refers to the dimensionless load–displacement relationship (skeleton curve) obtained by connecting the skeleton curves of each loop when the member is subjected to cyclic loading. It has been considered equivalent to the rotation capacity of the member under monotonic loading. Therefore, it is used as an index for evaluating the performance of members in the static incremental analysis (pushover analysis) of steel frame structures subjected to static seismic forces [64].

Conversely, in time–history response analyses, the energy dissipation of the hinge parts of columns and beams in the structure is used as an evaluation criterion [65]. The relationship between the energy dissipation capacity under monotonic loading and hysteretic energy dissipation is evaluated using the Bausinger effect coefficient, and different methods for assessing the performance of other members are used in seismic design analysis methods. The Bausinger effect coefficient is the ratio of the energy absorption in the softening zone during cyclic loading, which is not evaluated in the skeleton curve, to the energy absorption in the skeleton curve of the load–deformation history curve of the member subjected to cyclic loading. In the case of beams, a coefficient of 2.0 is set according to the recommendation of the Architectural Institute of Japan (AIJ). However, since the Bausinger effect varies with the loading amplitude and number of cycles [66,67], it is necessary to clarify the relationship between the energy dissipation capacity obtained from the skeleton curve and the hysteretic energy dissipation of the entire loading history. Otherwise, differences in mechanical performance may occur for the same member when different analysis methods are used. Therefore, it is necessary to ascertain the rotation and energy dissipation capacity of members constituting the main structure and clarify their relationship.

On the other hand, although experimental and analytical data on I-beams subjected to monotonic loading and cyclic loading have been collected in previous studies [68–77], the influence of the loading history on the rotation capacity, energy dissipation capacity, hysteretic energy dissipation, and Bausinger effect coefficient has not been clarified yet.

This paper aims to establish primary data on the history characteristics of I-beams subjected to monotonic loading and cyclic incremental loading by conducting loading experiments on I-beams with different loading histories, using the parameters of the flange width–thickness ratio and shear span-to-depth ratio. It collects experimental data on the structural performances at the maximum flexural strength time and stores the experimental results in a database. Then, based on the data extracted from earlier experimental studies [78–97], where the load–deformation relationship can be extracted as a cantilever beam type, the experimental results of I-beams which failed due to local buckling under monotonic loading and cyclic incremental loading are collected, and the data are databased. Differences in the width–thickness ratio, shear span-to-depth ratio, loading history, etc., are examined to clarify their effects on the ultimate strength ratio and energy dissipation capacity. Furthermore, for cyclic incremental loading, an evaluation equation for the Bausinger effect coefficient with the loading amplitude and number of loadings as parameters is proposed, and a performance evaluation method considering differences in loading history characteristics is presented.

The novel evaluation equation proposed and validated in this study realizes the proper reflection of the impact of various loading protocols (monotonic loading, repeated loading,

number of cycles) on the Bauschinger effect coefficient, even for beams with identical cross-sections and lengths. This enables the specification of the behavior of beams within an MRF, reaching their ultimate flexural strength contingent upon the stress history encountered during earthquakes.

2. Cyclic Loading Tests on I-Shaped Steel Beams with Different Flange Width-to-Thickness Ratios, Shear Span Ratios, and Loading Histories

2.1. Outline of Experiment on I-Beams

Figure 1 shows the test specimen for the loading experiment. A 2000 kN universal testing machine was used for the experiment, employing a three-point bending method. As shown in the figure, the left side of the loading point is reinforced with cover plates welded to the upper and lower flanges, and the loading beam is designed to maintain elasticity even when the test specimen reaches its maximum load. Table 1 lists the test specimens. In their designation, the first letter stands for the loading protocols (A: monotonic, B: cyclic, one loading cycle with a specific displacement, and C: cyclic, three loading cycles with a specific displacement), the second number denotes the flange width–thickness ratio (1: b/t_f = 6.25, 2: b/t_f = 4.17, and 3: b/t_f = 8.33), and the third number indicates the shear span-to-depth ratio (1: L/H = 5, L/H = 4, and L/H = 6).

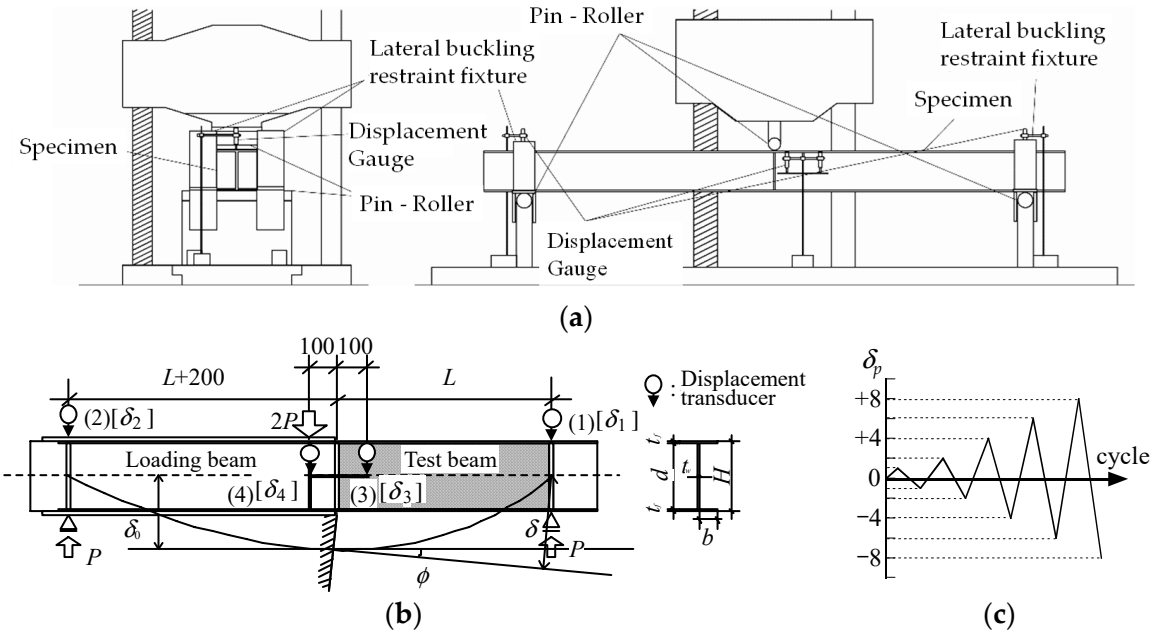

Figure 1. Outline of experiment and specimen: (**a**) testing apparatus; (**b**) measurements; (**c**) loading protocol (cyclic, one loading cycle with a specific displacement).

There are a total of 11 specimens, and SN400 steel was used for the specimens. The cross-section of the specimens has a web depth of 200 mm, a web thickness of 8 mm, and a flange thickness of 12 mm, with varying flange width-to-thickness ratios and shear span-to-depth ratios. This experiment selected beams with a small web depth-to-thickness ratio, for which there are few existing experimental results. The loading methods include monotonic and cyclic incremental loading, with the cyclic loading program designed based on the assumption of beams subjected to seismic forces. During an earthquake, when horizontal forces act on a moment-resisting frame, bending moments resulting from shear forces acting on the columns are transmitted to the beams. Given that the entire beam experiences an unsymmetric bending moment, the loading condition for half of the beams in the moment-resisting frame was adopted for this experiment. Figure 1c depicts the loading protocol for the cyclic loading experiments. The deformation δ_p corresponding to the full plastic bending moment M_p of the test specimen divided by the

beam length L was set as the criterion for cyclic loading, and one cycle of loading was repeated at each step of $\pm\delta_p$, $\pm 2\delta_p$, $\pm 4\delta_p$, and $\pm 6\delta_p$ of the incremental loading, except for specimen C-1-1. In contrast, for specimen C-1-1, three loading cycles were applied at each step. The M_p was calculated using the measured values shown in Table 2. As shown in Figure 1, one displacement transducer was installed at the position 100 mm from the center of the beam on both sides, and one displacement transducer was installed at each end support of the test specimen. The controlled displacement δ was calculated as a cantilever beam based on the displacement δ_0 at the position of the transducer and the rotation angle φ of the transducer.

$$\delta = \delta_0 + \varphi L = (\delta_3 + \delta_4)\frac{100}{200} - (\delta_1 + \delta_2)\frac{L}{2L + 200} + \left(\frac{\delta_3 - \delta_4}{200} - \frac{\delta_1 - \delta_2}{2L + 200}\right)L \quad (1)$$

Table 1. Test configurations.

Designation	L [mm]	b/t_f [mm]	d/t_w [mm]	L/H [-]	Slenderness Ratio [-]	Protocol	No. of Cycles
A-1-1	1000	6.25	22	4.95	24.55	Monotonic	-
B-1-1				4.95		Cyclic	1
C-1-1				4.98		Cyclic	3
A-2-1		4.17		4.98	37.88	Monotonic	1
B-2-1				4.95		Cyclic	1
A-3-1		8.33		4.98	18.15	Monotonic	1
B-3-1				4.95		Cyclic	1
A-1-2	800	6.25		3.96	19.64	Monotonic	1
B-1-2						Cyclic	1
A-1-3	1200			5.97	29.46	Monotonic	1
B-1-3						Cyclic	1

Table 2. Measurement of section dimensions.

Specimen	H [mm]	B [mm]	t_f [mm]	t_w [mm]
A-1-1	202	150	11.9	8.20
B-1-1	202	150	12.1	8.10
C-1-1	201	150	12.0	8.25
A-2-1	201	101	12.0	8.25
B-2-1	202	100	12.1	8.25
A-3-1	201	200	11.8	8.20
B-3-1	202	201	11.8	8.20
A-1-2	202	150	12.0	8.25
B-1-2	202	150	11.9	8.25
A-1-3	201	150	11.9	8.35
B-1-3	201	151	12.0	8.25

Here, δ_1 to δ_4 represent the vertical displacements of displacement transducers numbered (1) to (4) in Figure 1. Additionally, δ_p is calculated from the following equation as the sum of the displacements δ_{mp} due to bending deformation and δ_{sp} due to shear deformation as referenced in the previous literature [69]:

$$\delta_p = \delta_{mp} + \delta_{sp}, \delta_{mp} = \frac{P_p L^3}{3EI}, \quad \delta_{sp} = \frac{\kappa P_p L}{GA} \quad (2)$$

Here, δ_{mp} represents the displacement of the simply supported beam due to bending deformation when the plastic moment is reached at the loaded side beam end, and δ_{sp} represents the displacement of the simply supported beam due to shear deformation. Additionally, E is Young's modulus, I is the moment of inertia, A is the cross-sectional area, G is the shear modulus, and κ is the shape factor.

The test specimens were made of SN400B steel in Japan. Two specimens were extracted from a 12 mm thick flange and an 8 mm thick web for tensile testing. Stress–strain curves are illustrated in Figure 2, and Table 3 presents the characteristics of the tensile test results. It is noted that the yield stress level of the 12 mm thick plate is lower than that of the 8 mm thick plate, while their tensile strengths are nearly equal. The material test of the steel was conducted in accordance with JIS Z 2241 [98].

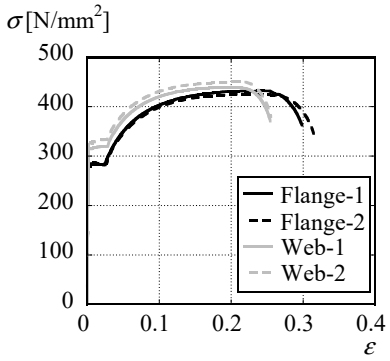

Figure 2. Stress–strain curves.

Table 3. Material test results.

	Thickness [mm]	E [N/mm^2]	σ_y [N/mm^2]	σ_u [N/mm^2]	Y.R.	Elongation [%]
Flange	8	1.99×10^6	323	444	0.727	21
Web	12	2.00×10^6	283	428	0.661	24

2.2. Plastic Deformation Characteristics of I-Beam with Different Loading Protocols

Figure 3a shows the load–displacement relationship of specimen C-1-1 subjected to cyclic loading. C-1-1 is a specimen subjected to loading three times with the same amplitude. The vertical axis represents the shear force acting on the beam P normalized by the ultimate plastic load P_p (=M_p/L), and the horizontal axis represents the displacement δ of the beam normalized by the displacement δ_p at the ultimate plastic strength.

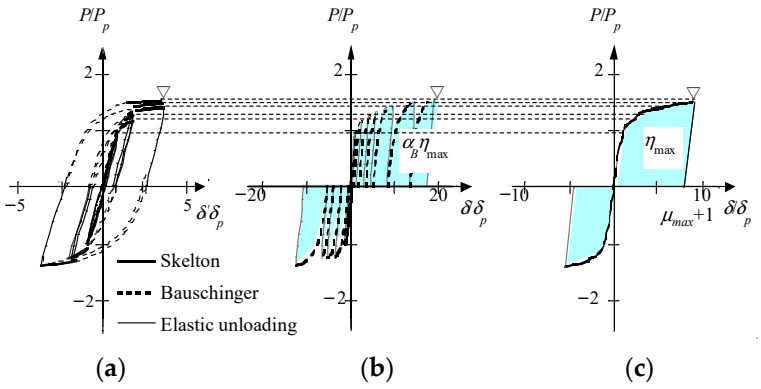

Figure 3. Procedure used to draw skeleton curve (C-1-1): (**a**) hysteresis curve; (**b**) cumulative hysteresis curve; (**c**) skeleton curve.

The cyclic load–displacement curve is divided into the skeleton curve, the Bauschinger effect region, and the elastic unloading region. The skeleton curve part is represented by thick solid lines corresponding to the load level experienced by the member for the first time. The Bauschinger effect region is defined by dashed lines corresponding to load levels previously experienced by the member. The elastic unloading region is represented by thin solid lines corresponding to the load level during unloading. The ▽ in the figure indicates the point of maximum strength.

Figure 3b shows the cumulative hysteresis curve of specimen C-1-1. The cumulative hysteresis curve decomposes the loading history curve into each loop. It connects the final displacement at the unloading of the previous loop and the initial displacement at the beginning of the next loop at $P/P_p = 0$ for each positive and negative loop. $\alpha_B \eta_{max}$ is the value obtained by subtracting the elastic deformation part from the total area up to the maximum strength in the cumulative history curve. It represents the dimensionless accumulated hysteretic energy dissipation.

Figure 3c shows the skeleton curve of specimen C-1-1. The skeleton curve connects only the skeleton curve part indicated by thick solid lines in the hysteresis curve of Figure 3a. In this paper, the value obtained by subtracting the elastic deformation part from δ_{max}/δ_p at the maximum strength is defined as the rotation capacity μ_{max} in the skeleton curve. The energy dissipation capacity η_{max} at the maximum strength in the skeleton curve is obtained by subtracting the elastic deformation part from the total area up to the maximum load and represents the dimensionless cumulative energy dissipation.

Here, α_B is the ratio of the energy dissipation capacity of the skeleton curve in Figure 3b to the hysteretic energy dissipation of the cumulative hysteresis curve in Figure 3c, which is the Bauschinger effect coefficient. The Bauschinger effect coefficient α_B is always greater than 1.

Figure 4 illustrates the load–displacement relationship for I-beams with equal cross-sections and lengths but different loading histories. Figure 4a shows the results of the cyclic loading tests, while Figure 4b shows the skeleton curves and results of the monotonic loading tests from Figure 4a. For the monotonic loading test A-1-1, the same history curve is drawn for both positive and negative sides. Even for specimens with the same shape, the skeleton curve of cyclic loading has a higher maximum strength and a smaller rotation capacity at the maximum strength compared to the load–displacement relationship of monotonic loading. This indicates that the skeleton curve obtained from cyclic loading is not necessarily equivalent to the load–displacement relationship of monotonic loading.

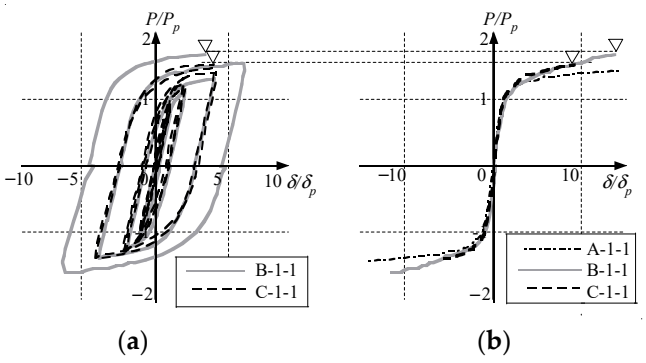

Figure 4. Comparison of test results of behavior under monotonic and cyclic loading: (**a**) hysteresis curve; (**b**) skeleton curve.

Figure 5 illustrates the strain distribution in the beam flange and web of specimen C-1-1 for the first, second, and third loading cycles with a loading amplitude $\delta/\delta_p = 3$. Figure 5a shows the strain distribution in the flange, with the upper side representing the compressive side and the lower side representing the tensile side. Figure 5b,c show the strain distribution in the web, with Figure 5b indicating the position 100 mm from the load point side of the specimen end and Figure 5c indicating the position 200 mm

from the load point side. At $\delta/\delta_p = 3$, local flange buckling has already occurred near the beam end during the first loading cycle, with some variation in strain values between the compressive and tensile flanges, but overall, they are nearly matched. As the loading cycles increase for the second and third cycles, the strain values increase in the plasticized region within 400 mm (2*H*) from the beam end. In other words, even at the same dimensionless displacement level, as the number of loading cycles increase, the strain values increase, and due to strain hardening, the stress also increases. Therefore, as shown in Figure 4, before local buckling occurs, the load on the skeleton curve of cyclic loading is higher at the same displacement compared to the load–displacement relationship of monotonic loading, and with more loading cycles, the load at the same displacement is slightly higher on the positive side.

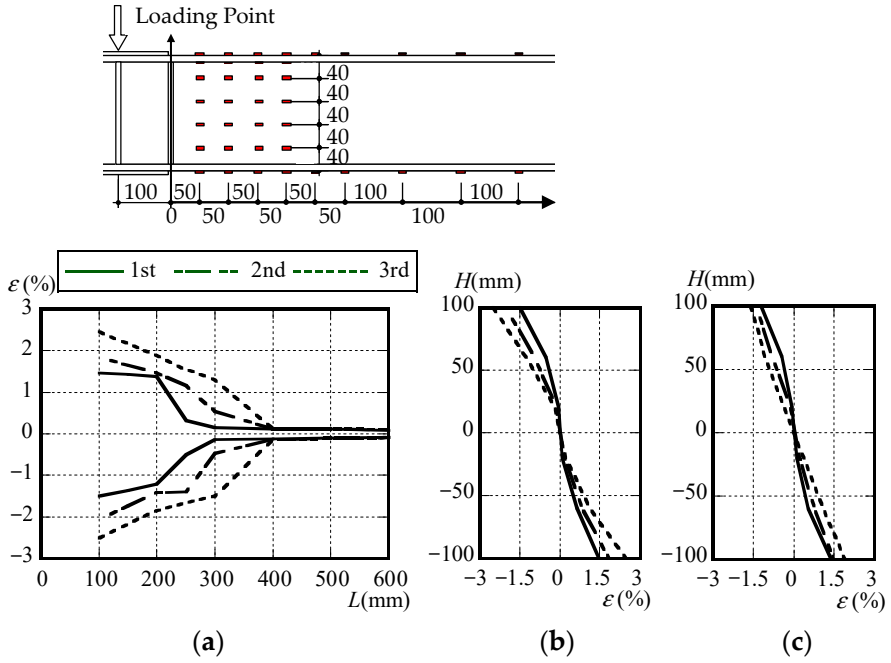

Figure 5. Strain distribution: (**a**) flange; (**b**) web (100 mm apart from fixed end); (**c**) web (200 mm apart from fixed end).

2.3. Influence of Loading Protocols on Cyclic Behavior of I-Beams

Table 4 presents a summary of the experimental results for all specimens. It includes the failure mechanism, the number of cycles at which local buckling occurred based on strain data, the rotation capacity μ_{max} in the skeleton curve, the energy dissipation capacity η_{max} in the skeleton curve, and the Bauschinger effect α_B. In cases where the flange width is narrow, such as specimens A-2-1 subjected to monotonic loading and B-2-1 subjected to cyclic loading, combined buckling occurred shortly after local buckling, leading to rapid strength degradation. Specimen B-3-1 experienced fracture due to welding defects at the welded joint between the longitudinal stiffener near the load point side and the tension flange after local buckling. On the other hand, in cases where the shear span-to-depth ratio is small, specimen A-1-2 reached its maximum strength due to local buckling, while specimen B-1-2 subjected to cyclic loading experienced flange local buckling due to bending moments, showing more prominent shear deformation compared to other specimens. Even for the specimens of the same section and length, different loading histories can result in different failure mechanisms.

Table 4. Summary of experimental results.

Specimen	Failure Modes	Cycle at Failure	μ_{max}	η_{max}	α_b
A-1-1	Local buckling		13.27	15.96	
B-1-1	Local buckling	$+2\delta_p$	12.65	16.16	2.06
C-1-1	Local buckling	$+2\delta_p$ (1st)	8.17	9.45	2.48
A-2-1	Combined buckling (local and lateral buckling)		8.34	7.96	
B-2-1	Combined buckling (local and lateral buckling)	$-4\delta_p$	8.64	13.84	1.63
A-3-1	Local buckling		11.86	13.33	
B-3-1	Local buckling and flange failure	$+2\delta_p$	5.46	10.41	1.61
A-1-2	Local buckling		20.90	26.59	
B-1-2	Combined buckling (local and shear buckling)	$+6\delta_p$	8.88	17.10	2.02
A-1-3	Local buckling		12.84	15.47	
B-1-3	Local buckling	$+2\delta_p$	7.85	14.09	1.82

Figure 6 illustrates the relationship between rotation capacity and energy dissipation capacity for I-beams with different flange width-to-thickness ratios and shear span ratios. Figure 6a,b depict the relationship between rotation capacity, energy dissipation capacity, and flange width-to-thickness ratio for monotonic and cyclic loading, while Figure 6c,d show the relationship between rotation capacity, energy dissipation capacity, and shear span-to-depth ratio. In Figure 6a,b, specimens with smaller width-to-thickness ratios (A-2-1 and B-2-1) experienced lateral buckling shortly after local buckling, resulting in a lower rotation capacity and energy dissipation capacity compared to specimens with larger width-to-thickness ratios (A-1-1 and B-1-1). However, for other specimens, the rotation capacity and energy dissipation capacity decreased as the width-to-thickness ratio increased. In Figure 6c,d, for specimens subjected to cyclic loading, specimen B-1-2 exhibited a lower rotation capacity due to significant shear deformation along with flange local buckling. However, for other specimens, the rotation capacity and energy dissipation capacity decreased as the shear span-to-depth ratio increased. Different buckling mechanisms between monotonic and cyclic loading indicate that cyclic loading induces local buckling in both flanges, leading to more advanced section deformation at the same loading displacement compared to monotonic loading, making it more susceptible to other buckling modes.

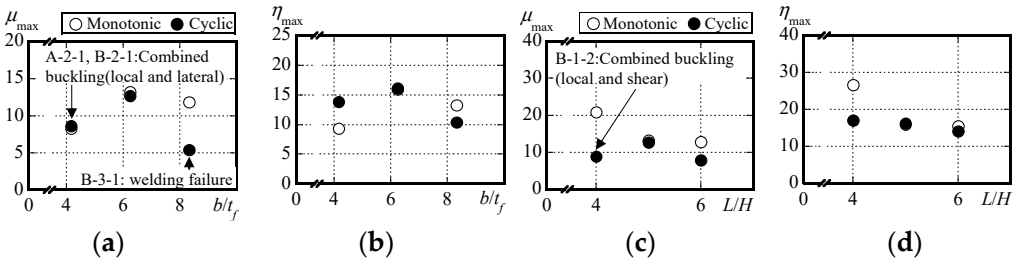

Figure 6. Relation between section dimensions and rotation capacity and energy dissipation capacity: (**a**) μ_{max} vs. b/t_f; (**b**) η_{max} vs. b/t_f; (**c**) μ_{max} vs. L/H; (**d**) η_{max} vs. L/H.

Figure 7 compares the experimental results of monotonic and cyclic loading for specimens with the same cross-section and length. Figure 7a–c show the ultimate strength ratio, rotation capacity, and energy dissipation capacity, respectively. Although the ultimate strength ratio is higher for cyclic loading in all specimens, the rotation capacity and energy

dissipation capacity are higher for monotonic loading, except for specimens A-2-1 and B-2-1, where the buckling mode was combined with lateral buckling. In the case of monotonic loading, local buckling occurs in the flanges subjected to compressive stress, while the flanges subjected to tensile stress experience plasticization and stretching. Under cyclic loading, the flange initially undergoes local buckling under compressive stress, followed by tension, resulting in extended local buckling deformation. Flanges subjected to tensile stress undergo plasticization and stretching, followed by local buckling under compressive stress. As a result, the stress state changes within the same loading amplitude, leading to pinching due to the alternating expansion and contraction of deformations. Consequently, even with the same displacement, cyclic loading causes a reduction in bearing capacity in a smaller deformation.

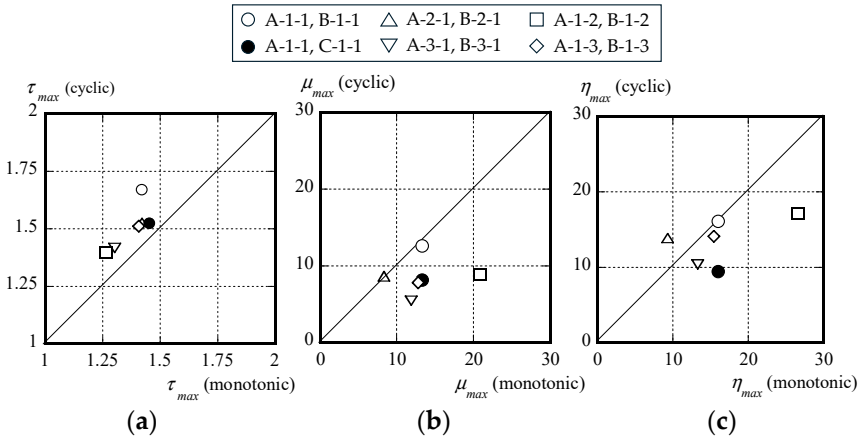

Figure 7. Comparison of experimental results under monotonic and cyclic loading: (**a**) τ_{max}; (**b**) μ_{max}; (**c**) η_{max}.

3. Rotation Capacity and Energy Dissipation Capacity of I-Beams That Failed Due to Local Buckling under Different Loading Protocols

3.1. Parameters of Experiment

Figure 8 illustrates the relationship between the width-to-thickness ratio of the test specimens from previous experiments [78–97] and the width-to-thickness ratio classification according to AISC, EC8-1, and AIJ codes [53,55,99,100]. The symbol ○ represents specimens from monotonic loading experiments, while ● represents specimens from the cyclic loading experiments. The test specimens are made of ordinary steel equivalent to either the 400 N/mm^2 class or the 490 N/mm^2 class. The figure shows 41 specimens from cyclic loading experiments for which history curves could be extracted, represented as ●, from previous articles [78–92] and 38 specimens from monotonic loading experiments, shown as ○, from earlier reports [93–97]. The relationship between each classification and rotation capacity is shown in Figure 8b. Additionally, the test specimens from this paper are denoted with a plus sign (+) for monotonic loading and a cross (×) for cyclic loading. Specimens where the maximum strength was reached due to lateral buckling (A-2-1 and B-2-1) and those fractured at welded joints (B-3-1) are excluded.

For instance, when comparing the width-to-thickness ratio of each beam with the Eurocode, both the flanges and webs display a broad spectrum of width-to-thickness ratios, spanning from Class 1 to Class 3, with the majority falling into Class 1. The web width-to-thickness ratios range approximately from 20 to 85, while the flange width-to-thickness ratios range from about 5 to 15. Notably, there was only one specimen for cyclic loading and two specimens for monotonic loading in the Class 4 equivalent rank.

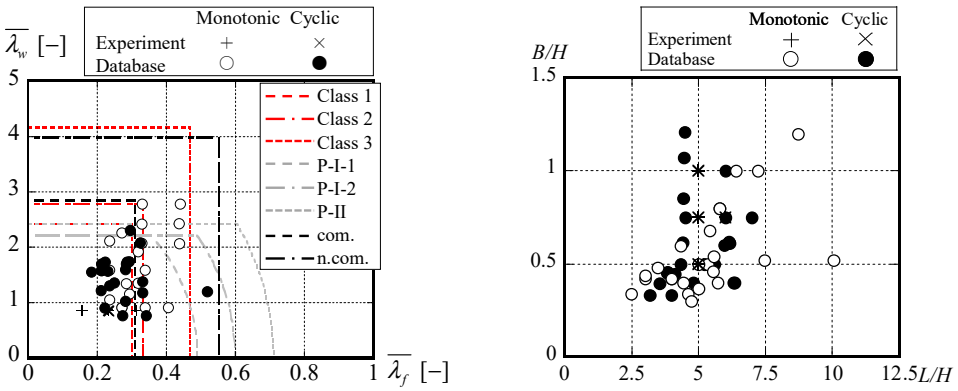

(**a**) (**c**)

EC		AIJ		AISC	
Class	Rotation capacity μ_{max}	Class	Rotation capacity μ_{max}	Class	Rotation capacity μ_{max}
Class 1	8 (7)	P-I-1	5 (4)	Compact	4 (3)
Class 2	3 (2)	P-I-2	3 (2)	Non-compact	1 (0)
Class 3	1 (0)	P-II	1 (0)	Slender	–
Class 4	–	P-III	–		

(**b**)

Figure 8. Distribution of specimen configuration: (**a**) width–thickness ratio; (**b**) rotation capacities depending on cross-section class; (**c**) section aspect ratio and shear span-to-depth ratio.

According to AISC [54], cross-sections classified as compact members must possess an inelastic rotation capacity (μ_{max}) equal to or greater than 3 (thus, a rotation capacity μ greater than 4). In contrast, EC 8-1 [99] mandates that cross-sections fall into Class 1, 2, or 3 for seismic design. Each class is associated with a specific behavior factor (q), with Class 1 requiring $q > 4$, Class 2 needing $q > 2$, and Class 3 stipulating $q > 1.5$. Conversely, EC 8-3 [100] specifies rotation capacity values of $\mu_{max} > 8$ for Class 1 and $\mu_{max} > 3$ for Class 2. Among the design codes, only the Japanese classification system outlined in AIJ [53] accounts for segment interaction. It comprises four classes (P-I-1, P-I-2, P-II, and P-III), with the required μ_{max} defined as follows: $\mu_{max} \geq 4$ for P-I-1, $\mu_{max} \geq 2$ for P-I-2, $\mu_{max} \geq 0$ for P-II, and $\mu_{max} < 0$ for P-III.

Figure 8c illustrates the relationship between the sectional aspect ratio and the shear span-to-depth ratio of I-beams. Here, the sectional aspect ratio refers to the ratio of beam width to height (B/H), and the shear span-to-depth ratio refers to the ratio of beam length to height (L/H). For hot-rolled members, these two indices can generally capture the section performance of I-beams and are used as indicators for section selection during design. Therefore, the figure shows the distribution of both indices. The sectional aspect ratio ranges from approximately 0.4 to 1.2, while the shear span-to-depth ratio ranges from about 2.5 to 10, within the range of hot-rolled I-beams used in actual structures.

3.2. Rotation Capacity, Ultimate Strength Ratio, and Energy Dissipation Capacity of I-Beams with Different Loading Protocols

Figure 9 organizes the experimental results of I-beams in terms of equivalent width-to-thickness ratio. The legend is the same as in Figure 8. Figure 9a illustrates the ultimate strength ratio, denoted as τ_{max} ($\tau_{max} = P_{max}/P_p$), while Figure 9b shows the rotation capacity, denoted as μ_{max}. The equivalent width-to-thickness ratio of I-beams is defined in Kadono et al. [101] by the following equation:

$$\left(\frac{b}{t_f}\right) = \sqrt{\frac{\sigma_{yf}}{E}\left(\frac{b}{t_f}\right)^2 + \frac{\sigma_{yw}}{41E}\left(\frac{d}{t_w}\right)^2} \quad (3)$$

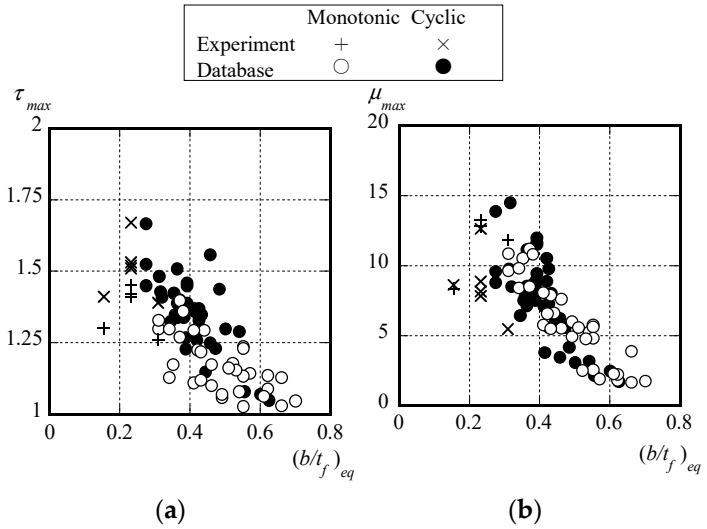

Figure 9. Width–thickness ratio and structural performance of I-beams; (**a**) ultimate strength ratio; (**b**) rotation capacity.

Here, σ_{yf} and σ_{yw} are the yield stresses of the flange and web, respectively, E is Young's modulus, and b/t_f and d/t_w are the flange width-to-thickness ratio and web width-to-thickness ratio, respectively.

Figure 9a,b show that as the equivalent width-to-thickness ratio decreases, the ultimate strength ratio τ_{max} and rotation capacity μ_{max} tend to increase. However, even for equal width-to-thickness ratios, the ultimate strength ratio is higher in the case of cyclic load experiments compared to monotonic load experiments, and the rotation capacity shows variability in the range from $(b/t_f)_{eq}$= 0.3 to 0.6.

Here are the experimental equations shown in a previous study [52], presented as Equations (4)–(6):

$$\tau_{max} = 1.46 - \left[0.63\frac{b}{t_f} + 0.053\frac{d}{t_w} + 0.02(\lambda_y - 50)\right]\sqrt{\varepsilon_y} \tag{4}$$

$$\mu_{max} = \frac{(\tau_{max} - 1)}{0.03} \tag{5}$$

$$\eta_{max} = \frac{(\tau_{max} + 1)(\mu_{max} + 1 - \tau_{max})}{2} \tag{6}$$

This paper considers the parameters of previous experimental equations and uses the least squares method to create experimental equations based on the results of 65 specimens from this experiment and the database outlined in Appendix A. Furthermore, considering the differences in loading methods, the number of repetitions and the repetition amplitude are added as parameters. The experimental equations proposed in this paper are shown in Equations (7)–(9):

$$\tau_{max} = \left[1.5 - 0.57\left(b/t_f\right)_{eq} - 0.010L/H\right]\left(1.1 - 0.1\frac{N}{\sum\mu_{xi}}\right) \tag{7}$$

$$\mu_{max} = \left[-7.2 + \frac{4.5}{\left(b/t_f\right)_{eq}} + \frac{8}{L/H}\right]\left(0.55 + 0.08\frac{\sum\mu_{xi}}{N}\right) - 1 \tag{8}$$

$$\eta_{max} = \frac{(\tau_{max} + 1)(\mu_{max} + 1 - \tau_{max})}{2} \tag{9}$$

In this context, N denotes the cumulative number of loading cycles until the attainment of the maximum load, where each loading cycle, whether positive or negative, contributes a value of 1. However, for instances of monotonic loading, N is stipulated to be 1. The symbol μ_{xi} represents the dimensionless amplitude of loading displacement in the i-th cycle.

In Equation (4), the flange-to-web thickness ratio, web thickness ratio, and yield strain are evaluated using the equivalent thickness ratio in Equation (7), with the aspect ratio being considered the shear span ratio.

Equation (5) previously comprised only the ultimate strength and axial force ratios (assumed as 0 here) to determine the plastic strain amplification. However, recognizing that rotation capacity is influenced not only by the thickness ratio but also by the proportion of the plasticization region [102], Equation (8) accounts for the effects of the equivalent thickness ratio and shear span-to-depth ratio. The rationale behind employing the shear span-to-depth ratio as an indicator of moment gradient lies in the disparity in the bending moments experienced by the flanges, even under equivalent moments. In cases of localized buckling failure, the local buckling of the flanges can impact the structural performance of the beam.

Figure 10 illustrates the correspondence between the experimental results from previous studies [78–97], the experimental results presented in this paper, as well as the experimental equations from both the earlier studies and the proposed equations in this paper. In Figure 10a, the comparison between the experimental results and the empirical equation (Equation (4)) from Kato's research [52] regarding the ultimate strength ratio is demonstrated. This paper aims to evaluate the mechanical performance of I-beams under cyclic loading by comparing them with the results of monotonic loading experiments and considering factors such as the number of cycles and load amplitudes, thereby enabling a consistent evaluation regardless of the loading conditions. It is noteworthy that compared to the experimental equations from previous studies, the experimental results generally exhibit larger values, particularly noticeable in the case of cyclic loading experiments. This discrepancy can be attributed to the fact that the experimental equations from previous studies do not consider the parameters of the cyclic loading history, thus not necessarily aligning well with the cyclic loading experimental results collected in this paper.

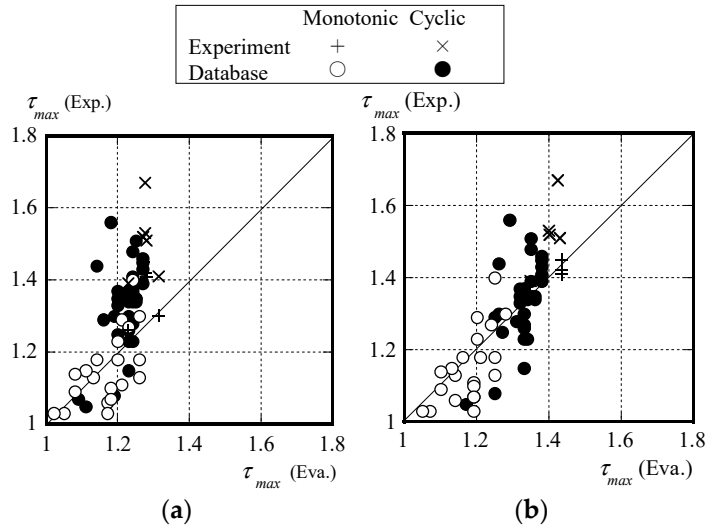

Figure 10. Comparison of ultimate strength ratio: (**a**) previous evaluation equation; (**b**) proposed evaluation equation.

Figure 10b presents a comparison between the experimental results of the ultimate strength ratio and the modified experimental equation (Equation (7)). Compared to the experimental equations from previous studies, the modified experimental equation proposed in this paper demonstrates better correspondence with the experimental results.

The error rates for the experimental equations from previous studies are 10.7% (12.6%) for Figure 10a and 6.1% (5.7%) for Figure 10b, while those for the modified experimental equations proposed in this paper are 6.1% (5.7%) and 6.1% (5.7%), respectively. This indicates a relatively good approximation of the experimental results for both monotonic and cyclic loading conditions. It is worth noting that the error rate is calculated by summing the differences between the experimental values and the values obtained from the experimental equations, divided by the total number of experimental data points, and expressed as a percentage. The first number in the error rate represents the case where both monotonic and cyclic loading experimental results are combined. In contrast, the number in parentheses represents the case where only cyclic loading experimental results are considered.

Figure 11 compares the experimental results of the rotation capacity, μ_{max}, with the experimental equations. Figure 11a utilizes the experimental equation (Equation (5)) from a previous study [52], while Figure 11b employs Equation (8). The shaded areas in the figures indicate the range of a 30% error for reference. Although there are no significant disparities between the experimental equations and the experimental results, the values of the experimental results vary widely around μ_{max} = 8 for the experimental equation (Equation (8)). On the other hand, Equation (8) demonstrates a generally good correspondence with the experimental results. The error rates for the experimental equation (Equation (5)) and Equation (8) are 31.3% (28.9%) and 23.1% (25.8%), respectively, indicating that using the experimental equations based on the equivalent thickness ratio and aspect ratio proposed in this paper can reduce the variability.

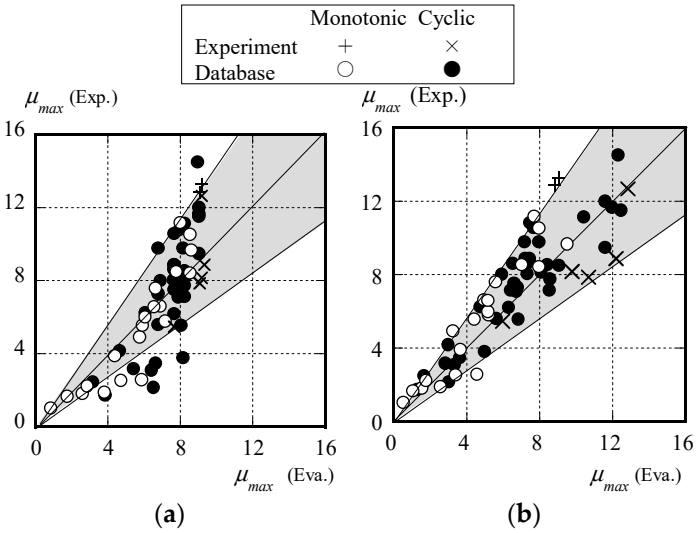

Figure 11. Comparison of rotation capacity: (**a**) previous evaluation equation; (**b**) proposed evaluation equation.

Figure 12 compares the experimental results of the energy dissipation capacity, η_{max}, with the experimental equations. Figure 12a,b employ the experimental equation (Equation (6)) from Kato's research [52] and Equation (9), respectively. The shaded areas in the figures indicate a 30% error range, similar to that in Figure 12. Meanwhile, the experimental equations from previous studies represent the gradient up to the maximum load, with a linear approximation. However, they may not correspond well with the experimental results obtained from Equations (4) and (5). Hence, several data points for η_{max} exceed the range of a 30% error, resulting in an error rate of 35.5% (36.1%). In contrast, the modified experimental equation proposed in this paper, Equation (9), demonstrates a better fit with many experimental results, falling within the 30% error range, resulting in an error rate of 25.2% (27.0%).

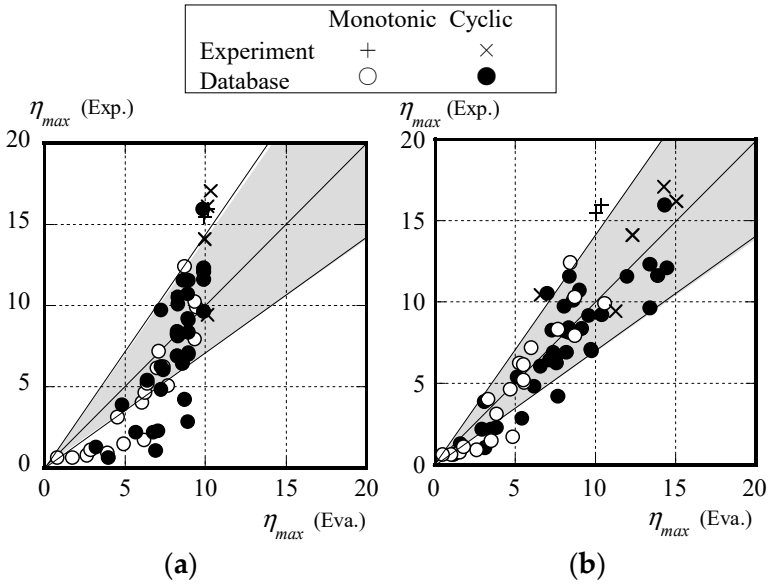

Figure 12. Comparison of energy dissipation capacity: (**a**) previous evaluation equation; (**b**) proposed evaluation equation.

In summary, by proposing experimental equations that consider parameters such as the equivalent thickness ratio, shear span-to-depth ratio, number of cycles up to the maximum load, and cumulative normalized displacement based on the parameters of previous experimental equations, this paper demonstrates that the experimental results can be more accurately represented.

3.3. Influence of Bauschinger Effect Coefficient of I-Beams That Failed Due to Local Buckling under Cyclic Loading

Figure 13 illustrates the relationship between the Bauschinger effect coefficient, the number of loading cycles, and the loading amplitude. The crosses represent the results of the cyclic loading experiments in this paper. Figure 13a depicts the relationship with the number of loading cycles N. In contrast, Figure 13b shows the relationship between the total dimensionless loading displacement amplitude $\sum \mu_{xi}$ and the Bauschinger effect coefficient α_B. The Bauschinger effect coefficient α_B is defined as the ratio of cumulative hysteretic energy dissipation in the cumulative hysteresis curve to the energy dissipation capacity in the skeleton curve, as described in earlier research [64], which is set to 2.0 for beams. While α_B shows an almost linear relationship with N and correlates with $\sum \mu_{xi}$, some variability is observed. Therefore, Figure 14 illustrates the relationship between both of the coefficients N and $\sum \mu_{xi}$ and the Bauschinger effect coefficient. The vertical axis represents the Bauschinger effect coefficient α_B, while the horizontal axis represents the variable used in the second term on the right-hand side of the equation.

$$\alpha_b = 1 + 0.5(N-1)\log\sqrt{\sum_{i=1} \mu_{xi}} \tag{10}$$

However, in the case of $N \leq 1$ (monotonic loading), N is set to 1. When the loading history remains within the elastic range during cyclic loading, only the first occurrence is counted.

From this paper and previous experimental results, it has been shown that this enhancement ratio depends on both the number of loading cycles and their amplitudes. Therefore, using both indicators in this paper, the evaluation equation is set as $\alpha_b = 1$ for monotonic loading and the above equation is formed through a trial-and-error method.

The plots in the figure represent the experimental results, while the dashed line corresponds to Equation (10). There is a tendency for the Bauschinger effect coefficient to increase with higher values of the total number of loading cycles and loading displacement amplitudes, and the experimental results generally agree with Equation (10).

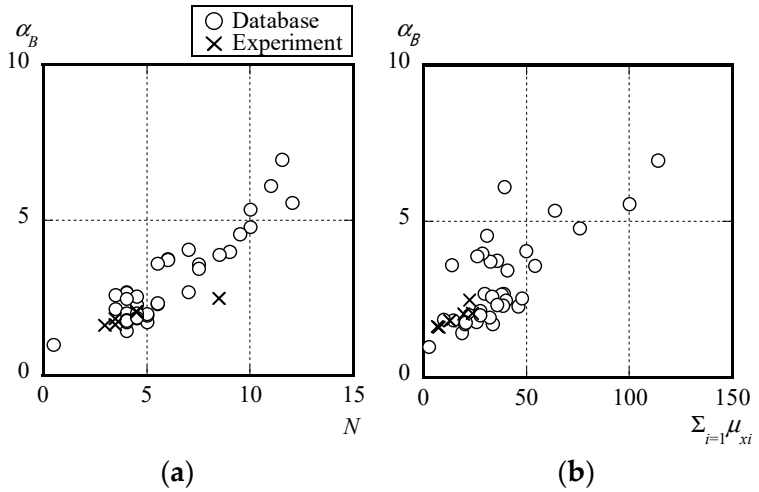

Figure 13. Relationship between Bauschinger effect coefficient and loading histories: (**a**) number of cycles; (**b**) cumulative plastic deformation.

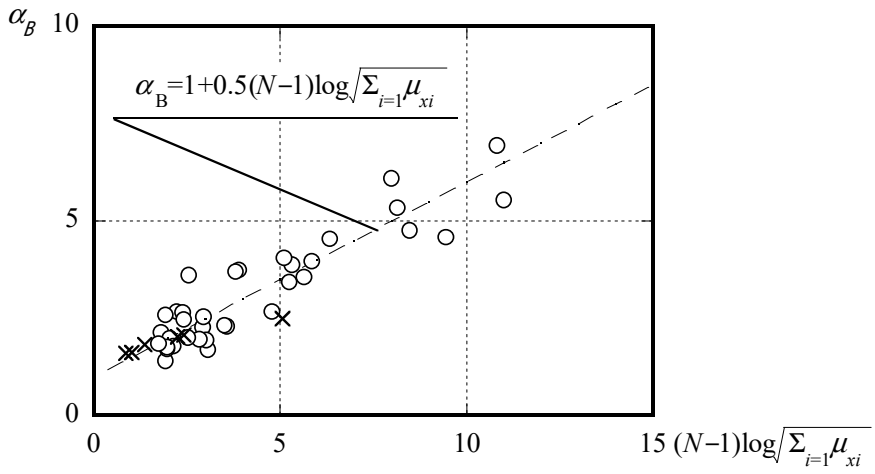

Figure 14. Evaluation of Bauschinger effect coefficient.

Thus, the hysteretic energy dissipation of an I-beam subjected to cyclic loading can be obtained by multiplying η_{max} obtained from Equation (9) by Equation (10).

In the field of structural engineering, numerous studies have focused on evaluating the performance of composite beams, where steel beams are attached to concrete slabs as composite members [27–33]. However, this paper focuses on the failure mechanism of steel beams, explicitly targeting the phenomenon of local buckling, and aims to evaluate the inherent performance of steel beams that failed due to local buckling. The performance evaluation of the composite beam will be clarified in a future study.

4. Conclusion

This paper elucidated the differences in the hysteresis curves and buckling mechanisms of locally buckling I-beams through monotonic and cyclic loading experiments. Subsequently, a simplified and accurate experimental equation was proposed based on the previous experimental equation as a unified evaluation method independent of loading

history differences. It is noteworthy that Table A1 comprises several specimens sharing identical cross-sectional shapes and lengths, yet lacks variation in loading protocols as a parameter. Therefore, concluding remarks (1) and (2) stem from the findings retrieved from the experiment in this study. The conclusions obtained are as follows:

(1) When subjected to cyclic loading at the same amplitude in the plastic region where local buckling occurs in I-beams, it was confirmed that the strain values increase and plasticization progresses as the number of cycles increase. When subjected to cyclic loading, the rotation capacity and energy dissipation capacity obtained from the experimental results decrease with increasing cycles at the same amplitude in the skeleton curve.
(2) For specimens of the same cross-section and length subjected to monotonic and cyclic loading, the rotation capacity and energy dissipation capacity are higher under monotonic loading if local buckling occurs.
(3) In the previous experimental equation, particularly in the case of cyclic loading, there are significant errors in the maximum load, rotation capacity, and energy dissipation capacity. On the other hand, the experimental equations proposed in this paper (Equations (7)–(9)) can generally evaluate the ultimate strength ratio, rotation capacity, and energy dissipation capacity regardless of the loading type.
(4) The Bauschinger effect coefficient increases with a more significant number of loading cycles and larger loading amplitudes, and its value can be evaluated using Equation (10). Moreover, hysteretic energy dissipation under cyclic loading can be assessed using Equations (9) and (10).

It should be noted that the application range of the experimental equations in this paper covers web-to-thickness ratios from 20 to 85, flange-to-thickness ratios from 5 to 15, section shape ratios from 0.4 to 1.2, and shear span-to-depth ratios from 2.5 to 10, based on the previous literature and the specimens tested in this paper.

This paper only targets the incremental amplitude type, and evaluating the performance of I-beams under decremental amplitude or random amplitude types is a future task.

Funding: This research study was funded by the Research Project of Co-Creation for Disaster Resilience (Principal Investigator: Yoshihiro Kimura). I express my deepest gratitude for their sincere support.

Data Availability Statement: The raw/processed data necessary to reproduce these findings cannot be shared at this time because the data also form part of an ongoing study.

Conflicts of Interest: The author declares that they have no known competing financial interests or personal relationships that could have appeared to influence the work reported in this paper.

Appendix A

The summary of the database obtained from previous articles is listed below. The hysteresis curves and residual deformation of all 11 specimens are presented below. All specimens except for A-2-1 and B-2-1 failed due to local buckling, while specimens A-2-1 and B-2-1 experienced coupled buckling induced by lateral buckling after local buckling, leading to ultimate failure. Specimen B-1-2 exhibited significant shear deformation in addition to bending deformation.

Table A1. Summary of database.

Section	L	b/t_f	d/t_w	L/H	τ_{max}	μ_{max}	η_{max}	N	$\Sigma\mu_{xi}$	Refs.
H-330 × 150 × 4.5 × 9	1260	8.3	69.3	3.8	1.29	3.21	2.24	11	39.07	[78]
H-330 × 150 × 4.5 × 9	1266	8.3	69.3	3.8	1.05	1.76	0.68	5.5	13.34	[78]
H-250 × 150 × 4.5 × 9	1496	8.3	51.6	6.0	1.25	3.5	2.33	9.5	30.49	[80]
H-250 × 150 × 4.5 × 12	1492	6.3	50.2	6.0	1.28	3.83	2.89	9	28.53	[80]
H-250 × 150 × 4.5 × 9	1497	8.3	51.6	6.0	1.3	3.13	2.22	8.5	25.91	[80]
H-250 × 150 × 4.5 × 9	1499	8.3	51.6	6.0	1.08	2.2	1.11	4.5	9.76	[80]
H-200 × 150 × 6 × 9	900	8.3	30.3	4.5	1.35	7.16	7.12	7	49.89	[81]
H-200 × 150 × 6 × 9	900	8.3	30.3	4.5	1.34	11.17	11.62	11.5	113.84	[81]
H-200 × 150 × 6 × 9	900	8.3	30.3	4.5	1.51	8.58	9.18	5.5	38.24	[81]
H-200 × 150 × 6 × 9	900	8.3	30.3	4.5	1.39	8.17	8.4	5.5	35.4	[81]
H-500 × 200 × 9 × 19	2400	5.3	51.3	4.8	1.23	5.6	4.23	27	130.71	[82]
H-450 × 200 × 9 × 12	1850	8.3	47.3	4.1	1.37	5.63	4.87	7.5	40.66	[83]
H-450 × 200 × 9 × 12	1850	8.3	47.3	4.1	1.35	9.82	9.78	12	99.8	[83]
H-450 × 200 × 9 × 12	1850	8.3	47.3	4.1	1.33	7.31	6.3	10	75.72	[83]
H-506 × 201 × 11 × 19	1800	5.3	42.5	3.6	1.35	7.77	7.05	4	29.42	[84]
H-300 × 130 × 6 × 12	1200	5.4	46.0	4.0	1.45	12.03	12.35	4	37.78	[85]
H-300 × 130 × 6 × 12	1200	5.4	46.0	4.0	1.45	11.54	12.15	4.5	47.62	[85]
H-300 × 130 × 6 × 12	1200	5.4	46.0	4.0	1.39	9.5	9.69	3.5	33.05	[85]
H-300 × 130 × 6 × 12	1200	5.4	46.0	4.0	1.46	11.69	11.66	4	39.85	[85]
H-300 × 100 × 9 × 9	1200	5.6	31.3	4.0	1.41	8.52	9.24	7	38.84	[86]
H-300 × 100 × 6 × 6	1200	8.3	48.0	4.0	1.44	4.2	3.9	4.5	14.18	[86]
H-488 × 300 × 11 × 18	2150	8.3	41.1	4.4	1.56	6.26	5.41	10	63.67	[87]
H-600 × 300 × 12 × 22	3125	6.8	46.3	5.2	1.36	7.18	6.48	5	25.28	[88]
H-600 × 300 × 12 × 22	3125	6.8	46.3	5.2	1.37	7.12	6.64	4	22.16	[88]
H-450 × 150 × 9 × 12	1425	6.3	47.3	3.2	1.35	8.06	6.08	6	32.4	[89]
H-250 × 125 × 6 × 9	1375	6.9	38.7	5.5	1.48	9.82	10.76	6	35.5	[90]
H-500 × 200 × 10 × 16	2168	6.3	46.8	4.3	1.34	10.85	11.59	7.5	53.87	[91]
H-500 × 200 × 10 × 16	3150	6.3	46.8	6.3	1.3	10.59	10.15	5	33.56	[92]
H-500 × 200 × 10 × 16	3150	6.3	46.8	6.3	1.26	8.9	8.15	5	31.85	[92]
H-500 × 200 × 10 × 16	3150	6.3	46.8	6.3	1.15	6.24	10.57	4	18.45	[92]
H-500 × 200 × 10 × 16	3175	6.3	46.8	6.4	1.37	8.7	8.44	4	25.51	[93]
H-500 × 200 × 10 × 16	3175	6.3	46.8	6.4	1.23	8.92	8.28	4.5	27.27	[93]
H-500 × 200 × 10 × 16	3175	6.3	46.8	6.4	1.27	8.65	8.3	4	19.91	[93]
H-500 × 200 × 10 × 16	3175	6.3	46.8	6.4	1.27	7.56	6.96	4	20.38	[93]
H-300 × 125 × 4.5 × 9	1200	6.9	62.7	4.0	1.29	6.65	6.3	-	-	[94]
H-300 × 125 × 9 × 9	1200	6.9	31.3	4.0	1.3	9.69	9.94	-	-	[94]
H-300 × 125 × 6 × 9	900	6.9	47	3.0	1.4	11.21	12.45	-	-	[94]
H-300 × 125 × 6 × 9	1200	6.9	47	4.0	1.27	8.55	8.33	-	-	[94]
H-180 × 144 × 6 × 9	1040	8.0	27	5.8	1.18	10.56	10.31	-	-	[95]
H-180 × 180 × 6 × 9	1300	10.0	27	7.2	1.11	5.81	5.11	-	-	[95]
H-180 × 216 × 6 × 9	1570	12.0	27	8.7	1.06	4.96	4.07	-	-	[95]
H-180 × 144 × 6 × 9	1040	8.0	27	5.8	1.13	8.46	7.98	-	-	[95]
H-300 × 180 × 6 × 9	1300	10.0	47	4.3	1.1	5.59	4.69	-	-	[95]
H-420 × 144 × 6 × 9	1040	8.0	67	2.5	1.07	6.03	5.23	-	-	[95]
H-420 × 144 × 6 × 9	1040	8.0	67	2.5	1.13	3.93	3.15	-	-	[95]
H-300 × 144 × 6 × 9	1040	8.0	47	3.5	1.03	2.6	1.77	-	-	[95]
H-270.5 × 108.5 × 4.23 × 5.57	1200	9.7	61.3	4.4	1.18	2.56	1.53	-	-	[96]
H-269.6 × 144.3 × 4.23 × 5.57	1500	13.0	61.1	5.6	1.09	1.86	0.81	-	-	[96]
H-314.4 × 108.3 × 4.23 × 5.57	1450	9.7	71.7	4.6	1.15	1.93	0.96	-	-	[96]
H-315.5 × 143.8 × 4.23 × 5.57	1750	12.9	72.0	5.5	1.03	1.69	0.66	-	-	[96]
H-359.7 × 108.8 × 4.23 × 5.57	1700	9.8	82.4	4.7	1.14	2.26	1.13	-	-	[96]
H-359.5 × 144.8 × 4.23 × 5.57	2050	13.0	82.4	5.7	1.03	1.78	0.68	-	-	[96]
H-250 × 125 × 5.8 × 8.5	1250	7.4	40.2	5.0	1.23	6.62	6.2	-	-	[97]
H-450 × 200 × 9 × 14	1350	7.1	46.9	3.0	1.18	7.62	7.22	-	-	[98]

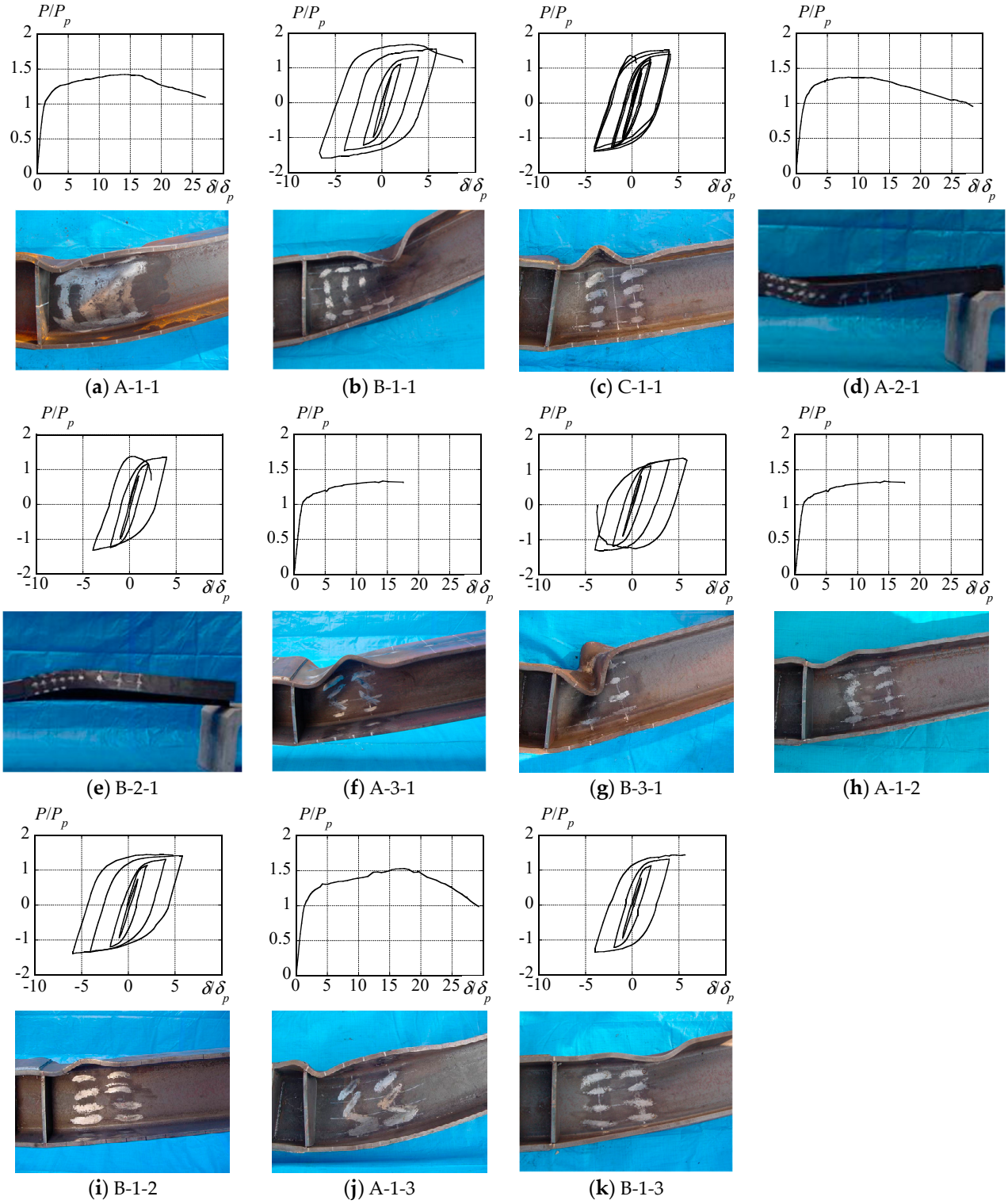

Figure A1. Load–displacement relationship and ultimate deformation state.

The list of symbols is presented below.

Table A2. List of symbols.

b/t_f	Flange width–thickness ratio
L/H	Shear span-to-depth ratio
L	Beam length
d/t_w	Web width-to-thickness ratio
H	Hight of beam
B	Width of beam
t_f	Flange thickness
t_w	Web thickness
δ_p	Displacement corresponding to full plastic bending moment
M_p	Full plastic bending moment
δ	Controlled displacement
δ_0	Displacement at position of transducer
φ	Rotation angle measured by the transducers
δ_{mp}	Displacements due to bending deformation of beam
δ_{sp}	Displacements due to shear deformation of beam
E	Young's modulus
I	Moment of inertia
A	Cross-sectional area
G	Shear modulus
κ	Shape factor
σ_y	Yield stress
σ_u	Tensile strength
Y.R.	Yield ratio (σ_y /σ_u)
P	Shear force acting on beam
P_p	Shear force imposing full plastic bending moment of beam
$\alpha_B\eta_{max}$	Hysteretic energy dissipation up to ultimate strength
α_B	Bauschinger effect coefficient
μ_{max}	Rotation capacity
η_{max}	Energy dissipation capacity
$\frac{b}{t_f}\sqrt{\frac{235}{\sigma_{yf}}}$	Generalized flange width-to-thickness ratio
$\frac{d}{t_w}\sqrt{\frac{235}{\sigma_{yw}}}$	Generalized web width-to-thickness ratio
B/H	Section aspect ratio
τ_{max}	Ultimate strength ratio
σ_{yf}	Yield stress of flange plate
σ_{yw}	Yield stress of web plate
N	Cumulative number of loading cycles until attainment of maximum load
μ_{xi}	Dimensionless amplitude of loading displacement in i-th cycle

References

1. Bleich, F. *Buckling Strength of Metal Structures*; McGraw Hill: New York, NY, USA, 1952.
2. Timoshenko, S.P. *Theory of Elastic Stability*; McGraw Hill: New York, NY, USA, 1963.
3. Nethercot, D.A.; Rockey, K.C. A Unified Approach to the Elastic Lateral Buckling of Beams. *Struct. Eng.* **1971**, *7*, 96–107. [CrossRef]
4. Narayanan, R. *Beam and Beam Columns-Stability and Strength*; Applied Science Publishers: Amsterdam, The Netherlands, 1983.
5. Salvador, T.G. Lateral Buckling of Eccentrically Loaded I—Columns. *Am. Soc. Civ. Eng.* **1956**, *121*, 1163–1179. [CrossRef]
6. Trahair, N.S. laterally unsupported beams. *Eng. Struct.* **1996**, *18*, 759–768. [CrossRef]
7. Nguyen, C.T.; Moon, J.; Lee, H.E. Lateral–torsional buckling of I-girders with discrete torsional bracings. *J. Constr. Steel Res.* **2010**, *66*, 170–177. [CrossRef]
8. Ji, X.L.D.; Twizell, S.C.; Driver, R.G.; Imanpour, A. Lateral Torsional Buckling Response of Compact I-Shaped Welded Steel Girders. *Eng. Struct.* **2022**, *148*, 04022149. [CrossRef]
9. Mohammadi, E.; Hosseini, S.S.; Rohanimanesh, M.S. Elastic lateral-torsional buckling strength and torsional bracing stiffness requirement for monosymmetric I-beams. *Eng. Struct.* **2016**, *104*, 116–125. [CrossRef]
10. Nguyen, C.T.; Joo, H.S.; Moon, J.; Lee, H.E. Flexural-torsional buckling strength of I-girders with discrete torsional braces under various loading conditions. *Eng. Struct.* **2022**, *36*, 337–350. [CrossRef]
11. Fukunaga, I.; Todaka, T.; Zhang, Z.; Kanao, I. Deformation Capacity of Wide Flange Beam with Lateral Bracings. *J. Struct. Constr. Eng. (Trans. AIJ)* **2022**, *87*, 372–380. (In Japanese) [CrossRef]
12. Bradford, M.A.; Gao, Z. Distortional buckling solutions for continuous composite beams. *J. Struct. Eng.* **1992**, *118*, 73–89. [CrossRef]

13. Kimura, Y.; Yoshino, Y. Required Bracing Capacity on Lateral Buckling Strength for H-Shaped Beams with Bracings. *J. Struct. Constr. Eng. (Trans. AIJ)* **2011**, *76*, 2143–2152. (In Japanese) [CrossRef]
14. Kimura, Y.; Yoshino, Y.; Ogawa, J. Effect of Lateral-Rotational Restraint and Strength of Continuously Braces on Lateral Buckling Load for H-Shaped Beams. *J. Struct. Constr. Eng. (Trans. AIJ)* **2013**, *78*, 193–201. (In Japanese) [CrossRef]
15. Kimura, Y.; Yoshino, Y. Effect of Lateral and Rotational Restraint for Bracings on Lateral Buckling Load for H-Shaped Beams under Moment Gradient. *J. Struct. Constr. Eng. (Trans. AIJ)* **2014**, *79*, 761–770. (In Japanese) [CrossRef]
16. Kimura, Y.; Matsuo, T.; Yoshino, Y. Estimation of Elasto-Plastic Lateral Buckling Stress for H-shaped Beams with Lateral Rotational Braces on subjected to Axial Force and Flexural Moment. *J. Struct. Constr. Eng. (Trans. AIJ)* **2014**, *79*, 1299–1308. (In Japanese) [CrossRef]
17. Kimura, Y.; Yoshino, Y. Effect of Lateral-Rotational Restraint of Continuous Braces on Lateral Buckling Strength for H-Shaped Beams with Flexural Moment Gradient. *J. Struct. Constr. Eng. (Trans. AIJ)* **2016**, *81*, 1309–1319. (In Japanese) [CrossRef]
18. Kimura, Y.; Sugita, Y.; Yoshino, Y. Effect of Lateral-Rotational Restraint of Continuous Braces on Lateral Buckling Strength for H-shaped Beams with Compressive Axial Force and Flexural Moment. *J. Struct. Constr. Eng. (Trans. AIJ)* **2016**, *81*, 1321–1331. (In Japanese) [CrossRef]
19. Kimura, Y.; Sugita, Y. Effect of Lateral-Rotational Restraint of Continuous Braces on Lateral Buckling Strength for H-shaped Beams with Gradient Flexural Moment and Compressive Axial Force. *J. Struct. Constr. Eng. (Trans. AIJ)* **2016**, *82*, 1799–1809. (In Japanese) [CrossRef]
20. Kimura, Y.; Miya, M.; Liao, W. Effect of Restraint for Continuous Braces on Lateral Buckling Load for H-shaped Beams with Warping Restraint of Beams to Column Joint. *J. Struct. Constr. Eng. (Trans. AIJ)* **2018**, *81*, 1353–1363. (In Japanese) [CrossRef]
21. Kimura, Y.; Miya, M. Effect of Warping Restraint of Beams to Column Joint on Lateral Buckling Behavior for H-Shaped Beams with Continuous Braces under Gradient Flexural Moment. *J. Struct. Constr. Eng. (Trans. AIJ)* **2019**, *84*, 1601–1611. (In Japanese) [CrossRef]
22. Kimura, Y.; Sato, Y. Effect of Warping Restraint of Beams to Column Joint on Lateral Buckling Behavior for H-Shaped Beams with Continuous Braces under Gradient Flexural Moment. *J. Struct. Constr. Eng. (Trans. AIJ)* **2021**, *86*, 145–155. (In Japanese) [CrossRef]
23. Yoshino, Y.; Liao, W.; Kimura, Y. Restraint effect on lateral buckling load of continuous braced H-shaped beams based on partial frame loading tests. *J. Struct. Constr. Eng. (Trans. AIJ)* **2022**, *87*, 634–645. (In Japanese) [CrossRef]
24. Kimura, Y.; Sato, Y.; Suzuki, A. Effect of Fork Restraint of Column on Lateral Buckling Behavior for H-Shaped Beams with Continuous Braces under Flexural Moment Gradient. *J. Struct. Constr. Eng. (Trans. AIJ)* **2022**, *87*, 316–327. (In Japanese) [CrossRef]
25. Yoshino, Y.; Kimura, Y. Rotational Stiffening Performance of Roof Folded Plates in Torsion Tests and the Stiffening Effect of Roof Folded Plates on the Lateral Buckling of H Beams in Steel Structures. *Buildings* **2024**, *14*, 1158. [CrossRef]
26. Rossi, A.; Nicoletti, R.S.; de Souza, A.S.C.; Martins, C.H. Lateral distortional buckling in steel-concrete composite beams: A review. *Structures* **2020**, *27*, 1299–1312. [CrossRef]
27. Suzuki, A.; Kimura, Y. Cyclic behavior of component model of composite beam subjected to fully reversed cyclic loading. *J. Struct. Eng.* **2019**, *145*, 04019015. [CrossRef]
28. Suzuki, A.; Abe, K.; Kimura, Y. Restraint performance of stud connection during lateral-torsional buckling under synchronized in-plane displacement and out-of-plane rotation. *J. Struct. Eng.* **2020**, *146*, 04020029. [CrossRef]
29. Suzuki, A.; Abe, K.; Suzuki, K.; Kimura, Y. Cyclic behavior of perfobond-shear connectors subjected to fully reversed cyclic loading. *J. Struct. Eng.* **2021**, *147*, 04020355. [CrossRef]
30. Suzuki, A.; Suzuki, K.; Kimura, Y. Ultimate shear strength of perfobond shear connectors subjected to fully reversed cyclic loading. *Eng. Struct.* **2021**, *248*, 113240. [CrossRef]
31. Suzuki, A.; Kimura, K. Mechanical performance of stud connection in steel-concrete composite beam under reversed stress. *Eng. Struct.* **2021**, *249*, 113338. [CrossRef]
32. Suzuki, A.; Hiraga, K.; Kimura, Y. Mechanical performance of puzzle-shaped shear connectors subjected to fully reversed cyclic stress. *J. Struct. Eng.* **2023**, *149*, 04023087. [CrossRef]
33. Suzuki, A.; Hiraga, K.; Kimura, Y. Cyclic behavior of steel-concrete composite dowel by clothoid-shaped shear connectors under fully reversed cyclic stress. *J. Adv. Concr. Technol.* **2023**, *21*, 76–91. [CrossRef]
34. Bedair, O. Stability of web plates in W-shape columns accounting for flange/web interaction. *Thin-Walled Struct.* **2009**, *47*, 768–775. [CrossRef]
35. Roberts, T.M.; Jhita, P.S. Lateral, local and distortional buckling of I-beams. *Thin-Walled Struct.* **1983**, *1*, 289–308. [CrossRef]
36. Bradford, M.A.; Hancock, G.J. Elastic interactions of local and lateral buckling in beams. *Thin-Walled Struct.* **1984**, *2*, 1–25. [CrossRef]
37. Chin, C.K.; Al-Bermani, F.G.A.; Kitipornchai, S. Stability of thin-walled members having arbitrary flange shape and flexible web. *Eng. Struct.* **1990**, *141*, 121–132. [CrossRef]
38. Seif, M.; Schafer, B.W. Local buckling of structural steel shapes. *J. Construct. Steel Res.* **2010**, *66*, 1232–1247. [CrossRef]
39. Han, K.H.; Lee, C.H. Elastic flange local buckling of I-shaped beams considering effect of web restraint. *Thin-Walled Struct.* **2016**, *105*, 101–111. [CrossRef]
40. Gardner, L.; Fieber, A.; Macorini, L. Formulae for calculating elastic local buckling stresses of full structural cross-sections. *Structures* **2019**, *17*, 2–20. [CrossRef]

41. Tankova, T.; da Silva, L.S.; Marques, L.; Tankova, T.; da Silva, L.S.; Marques, L. Buckling resistance of non-uniform steel members based on stress utilization: General formulation. *J. Construct. Steel Res.* **2019**, *149*, 239–256. [CrossRef]
42. Ragheb, W.F. Local buckling of welded steel I-beams considering flange–web interaction. *Thin-Walled Struct.* **2015**, *97*, 241–249. [CrossRef]
43. Gioncu, V. Framed structures. Ductility and seismic response: General Report. *J. Constr. Steel Res.* **2000**, *55*, 125–154. [CrossRef]
44. Gioncu, V.; Mosoarca, M.; Anastasiadis, A. Prediction of available rotation capacity and ductility of wide-flange beams: Part 1: DUCTROT-M computer program. *J. Constr. Steel Res.* **2011**, *69*, 8–19. [CrossRef]
45. Anastasiadis, A.; Mosoarca, M.; Gioncu, V. Prediction of available rotation capacity and ductility of wide-flange beams: Part 2: Applications. *J. Constr. Steel Res.* **2011**, *68*, 176–191. [CrossRef]
46. Shokouhian, M.; Shi, Y. Classification of I-section flexural members based on member ductility. *J. Constr. Steel Res.* **2014**, *95*, 198–210. [CrossRef]
47. Araujo, M.; Macedo, L.; Castro, J. Evaluation of the rotation capacity limits of steel members defined in EC8-3. *J. Constr. Steel Res.* **2017**, *135*, 11–29. [CrossRef]
48. Cardoso, D.; Vieira, J. Comprehensive local buckling equations for FRP I-sections in pure bending or compression. *Compos. Struct.* **2017**, *182*, 301–310. [CrossRef]
49. Ascione, F.; Feo, L.; Lamberti, M.; Minghini, F.; Tullini, N. A closed-form equation for the local buckling moment of pultruded FRP I-beams in major-axis bending. *Compos. Part B* **2016**, *97*, 292–299. [CrossRef]
50. Qiao, P.; Davalos, J.; Wang, J. Local Buckling of Composite FRP Shapes by Discrete Plate Analysis. *J. Struct. Engineering. Am. Soc. Civ. Eng.* **2001**, *127*, 245–255. [CrossRef]
51. Torabian, S.; Schafer, B. Role of local slenderness in the rotation capacity of structural steel members. *J. Constr. Steel Res.* **2013**, *95*, 32–43. [CrossRef]
52. Kato, B.; Akiyama, H.; Obi, Y. Deformation characteristics of H-shaped steel members influenced by local buckling. *J. Struct. Constr. Eng. (Trans. AIJ)* **1997**, *257*, 49–57. (In Japanese)
53. Architectural Institute of Japan (AIJ). *Recommendation for Limit State Design of Steel Structures*; Maruzen Publishing Co., Ltd.: Tokyo, Japan, 2010. (In Japanese)
54. American Institute of Steel Construction (AISC). *Seismic Provisions for Structural Steel Buildings*; AISC: Chicago, IL, USA, 2016.
55. Architectural Institute of Japan (AIJ). *AIJ Recommendations for Plastic Design of Steel Structures*; Maruzen Publishing Co., Ltd.: Tokyo, Japan, 2017. (In Japanese)
56. Lignos, D.G.; Krawinkler, H. *Sidesway Collapse of Deteriorating Structural Systems under Seismic Excitations*; Report No. TB 172; The John A. Blume Earthquake Engineering Center, Stanford University: Stanford, CA, USA, 2009.
57. Lignos, D.G.; Krawinkler, H. A steel database for component deterioration of tubular hollow square steel columns under varying axial load for collapse assessment of steel structures under earthquakes. In Proceedings of the 7th International Conf. on Urban Earthquake Engineering (7CUEE), Tokyo, Japan, 3–5 March 2010.
58. Lignos, D.G.; Laura Eads Krawinkler, H. Effect of Composite Action on the Dynamic Stability of Special Steel Moment Resisting Frames Designed in Seismic Regions. In Proceedings of the ASCE Structures Congress, Budapest, Hungary, 31 August–2 September 2011.
59. Lignos, D.G.; Krawinkler, H. Deterioration modeling of steel components in support of collapse prediction of steel moment frames under earthquake loading. *J. Struct. Eng.* **2011**, *137*, 1291–1302. [CrossRef]
60. Lignos, D.G.; Krawinkler, H.; Whittaker, A. Prediction and validation of sidesway collapse of two scale models of a 4-story steel moment frame. *J. Earthq. Eng. Struct.* **2011**, *40*, 807–825. [CrossRef]
61. Lignos, D.G.; Hikino, T.; Matsuoka, Y.; Nakashima, M. Collapse Assessment of Steel Moment Frames Based on E-Defense Full-Scale Shake Table Collapse Tests. *J. Struct. Eng.* **2013**, *139*, 120–132. [CrossRef]
62. Kanao, I.; Nakashima, M.; Takehara, S. Braced frame model considering buckling and fracture and its responses under near-fault strong motions. *J. Struct. Constr. Eng. (Trans. AIJ)* **2004**, *577*, 117–122. (In Japanese) [CrossRef] [PubMed]
63. Uang, C.M.; Yu, Q.S.; Gilton, C.S. Effects of loading history on cyclic performance of steel RBS moment connections. In Proceedings of the 12th World Conference on Earthquake Engineering, Auckland, New Zealand, 30 January–4 February 2000.
64. Architectural Institute of Japan (AIJ). *Ultimate Strength and Deformation Capacity of Building in Seismic Design (1990)*; Maruzen Publishing Co., Ltd.: Tokyo, Japan, 1990. (In Japanese)
65. Architectural Institute of Japan (AIJ). *Evaluation Procedure for Performance-Based Design of Buildings-Calculation of Response and Limit Strength, Energy Balance-Based Seismic Resistant Design, Time History Response Analysis*; AIJ: Tokyo, Japan, 2005. (In Japanese)
66. Shimazu, M.; Kimura, Y. Correlation between plastic deformation capacity and energy absorption capacity for H-shaped beams with local buckling. In *Summaries of Technical Papers of Annual Meeting Architectural Institute of Japan*; Japan Society for Finishings Technology: Tokyo, Japan, 2006; pp. 845–846. (In Japanese)
67. Shimazu, M.; Kimura, Y. Effects of flange width-to-thickness ratio and shear span ratio of plastic deformation capacity and energy absorption capacity for H-shaped beams. In *Summaries of Technical Papers of Annual Meeting Architectural Institute of Japan*; Japan Society for Finishings Technology: Tokyo, Japan, 2007; pp. 627–628. (In Japanese)
68. Qi, H.; Tada, M.; Tani, N.; Shirai, Y. Monotonic and hysteretic model for H-shaped beams incorporating deterioration behavior owing to the local buckling. *Thin-Walled Struct.* **2020**, *157*, 107016. [CrossRef]

69. Kimura, Y.; Yamanishi, T.; Kasai, K. Cyclic Hysteresis Behavior and Plastic Deformation Capacity for H-shaped Beams on Local Buckling under Compressive and Tensile Forces. *J. Struct. Constr. Eng. (Trans. AIJ)* **2013**, *78*, 1307–1316. (In Japanese) [CrossRef]
70. Kimura, Y.; Suzuki, A.; Kasai, K. Estimation of plastic deformation capacity for H-shaped beams on local buckling under compressive and tensile forces. *J. Struct. Constr. Eng. (Trans. AIJ)* **2016**, *81*, 2133–2142. (In Japanese) [CrossRef]
71. Suzuki, A.; Kimura, Y.; Kasai, K. Plastic deformation capacity of H-shaped beams collapsed with combined buckling under reversed axial forces. *J. Struct. Constr. Eng. (Trans. AIJ)* **2018**, *83*, 297–307. (In Japanese) [CrossRef]
72. Suzuki, A.; Kimura, Y.; Kasai, K. Rotation capacity of I-shaped beams under alternating axial forces based on buckling-mode transitions. *J. Struct. Eng.* **2020**, *146*, 04020089. (In Japanese) [CrossRef]
73. Kimura, Y.; Fujak, S.M.; Suzuki, A. Elastic local buckling strength of I-beam cantilevers subjected to bending moment and shear force based on flange-web interaction. *Thin-Walled Struct.* **2021**, *162*, 107633. [CrossRef]
74. Fujak, S.M.; Kimura, Y.; Suzuki, A. Estimation of elastoplastic local buckling capacities and novel classification of I-beams based on beam's elastic local buckling strength. *Structures* **2022**, *39*, 765–781. [CrossRef]
75. Fujak, S.M.; Suzuki, A.; Kimura, Y. Estimation of ultimate capacities of Moment-Resisting Frame's subassemblies with Mid-Storey Pin connection based on elastoplastic local buckling. *Structures* **2023**, *48*, 410–426. [CrossRef]
76. Suzuki, A.; Kimura, Y. Rotation capacity of I-shaped beam failed by local buckling in buckling-restrained braced frames with rigid beam-column connections. *J. Struct. Eng.* **2023**, *149*, 04022243. [CrossRef]
77. Suzuki, A.; Kimura, Y.; Matsuda, Y.; Kasai, K. Rotation capacity of I-shaped beams with concrete slab in buckling-restrained braced frames. *J. Struct. Eng.* **2024**, *150*, 04023204. [CrossRef]
78. Fujikawa, T.; Fujiwara, K. Research on strength and deformation capacity of H-shaped beam under cyclic loading. In *Proceedings of Architectural Institute of Japan Kinki Chapter Research Meeting*; AIJ: Tokyo, Japan, 1984; pp. 337–340. (In Japanese)
79. Fujiwara, K.; Kato, S. A study on deformation capacity of H-shaped steel beams with relative large ratio of web depth to thickness under cyclic loading. In *Proceedings of Architectural Institute of Japan Kinki Chapter Research Meeting*; AIJ: Tokyo, Japan, 1985; pp. 425–428. (In Japanese)
80. Sakai, J.; Matsui, C.; Kuno, T. Effects of the difference of the value of yield ratio of steel and the collapse-types of frame on the ductility of steel frame. In *Summaries of Technical Papers of Annual Meeting Architectural Institute of Japan*; Japan Society for Finishings Technology: Tokyo, Japan, 1990; pp. 1351–1352. (In Japanese)
81. Fujita, T.; Nakagomi, T.; Mizusaki, Y. The experimental research concern with structural behaviors of welded beam-to-column connections using cold-formed square steel tube column. In *Summaries of Technical Papers of Annual Meeting Architectural Institute of Japan*; Japan Society for Finishings Technology: Tokyo, Japan, 1992; pp. 1537–1538. (In Japanese)
82. Kai, S.; Sera, K.; Abukawa, T.; Yabe, Y.; Terada, G. Structural behavior of H-shaped beam-end connected to RHS-column. In *Summaries of Technical Papers of Annual Meeting Architectural Institute of Japan*; Japan Society for Finishings Technology: Tokyo, Japan, 1992; pp. 1541–1542. (In Japanese)
83. Makishi, T.; Yamamoto, N.; Tsutsui, S.; Fujisawa, K.; Uemori, H.; Ishii, T.; Morita, K. Experimental study on the deformation capacity of welded beam end connection without weld access hole. In *Summaries of Technical Papers of Annual Meeting Architectural Institute of Japan*; Japan Society for Finishings Technology: Tokyo, Japan, 1993; pp. 1257–1260. (In Japanese)
84. Ito, H.; Kimura, M.; Kaneko, H.; Yagi, T.; Ishii, H. Experimental study on beam-to-column welding connection without beam scallops. In *Summaries of Technical Papers of Annual Meeting Architectural Institute of Japan*; Japan Society for Finishings Technology: Tokyo, Japan, 1993; pp. 1261–1262. (In Japanese)
85. Suzuki, T.; Motoyui, S.; Fukazawa, T.; Uchikoshi, T. Study on effect of width-thickness ratio on deformation capacity of beams with scallops. *J. Struct. Constr. Eng. (Trans. AIJ)* **1996**, *486*, 107–114. (In Japanese) [CrossRef] [PubMed]
86. KMinami; Fujita, T.; Sasaki, Y. Experimental study on effect of non-scallops on deformation capacities of beam-to-column welded joints. In *Summaries of Technical Papers of Annual Meeting Architectural Institute of Japan*; Japan Society for Finishings Technology: Tokyo, Japan, 1996; pp. 631–632. (In Japanese)
87. Ishimaru, R.; Kagami, S.; Tanaka, A.; Masuda, K. Experimental study on the statical characteristics of the WBFW type beam-to-column connections. In *Summaries of Technical Papers of Annual Meeting Architectural Institute of Japan*; Japan Society for Finishings Technology: Tokyo, Japan, 1997; pp. 429–430. (In Japanese)
88. Sawamoto, Y.; Yoshida, H.; Kihiara, H.; Torii, S.; Tanaka, N. Experimental study on detail of H-shaped beam-to-box column connection. In *Summaries of Technical Papers of Annual Meeting Architectural Institute of Japan*; Japan Society for Finishings Technology: Tokyo, Japan, 1998; pp. 375–376. (In Japanese)
89. Yasuno, T.; Tsujioka, S.; Tada, M. Alternate loading test of haunch-beams made from rolled wide-flange shape. In *Summaries of Technical Papers of Annual Meeting Architectural Institute of Japan*; Japan Society for Finishings Technology: Tokyo, Japan, 2001; pp. 583–586. (In Japanese)
90. Kamaga, H.; Makino, Y.; Kuroba, K.; Tanaka, M.; Fukudome, Y.; Kobukuro, Y. Testing of beam-to-RHS column connections with-out weld access holes for field welding. In *Summaries of Technical Papers of Annual Meeting Architectural Institute of Japan*; Japan Society for Finishings Technology: Tokyo, Japan, 2001; pp. 919–922. (In Japanese)
91. Nakano, T.; Masuda, H.; Sasaji, T.; Tanaka, A. Experimental study on behavior of WBFW type beam-to-column connection. *J. Struct. Constr. Eng. (Trans. AIJ)* **2002**, *556*, 139–144. (In Japanese) [CrossRef] [PubMed]
92. Nakano, T.; Masuda, H.; Tanaka, A. Experimental study on effect of reinforcements at web connected parts of WF beam to SHS column connections. *J. Struct. Constr. Eng. (Trans. AIJ)* **2003**, *566*, 145–152. (In Japanese) [CrossRef] [PubMed]

93. Suzuki, T.; Ono, T.; Kanebako, Y. The local buckling and inelastic deformation capacity of steel beams under shear bending. *J. Struct. Constr. Eng. (Trans. AIJ)* **1977**, *260*, 91–98. (In Japanese)
94. Kato, T.; Akiyama, H.; Obi, Y. Experimental study of H-shaped beam with relatively large width-thickness ratio on local buckling characteristics. In *Summaries of Technical Papers of Annual Meeting Architectural Institute of Japan*; Japan Society for Finishings Technology: Tokyo, Japan, 1976; pp. 1075–1076. (In Japanese)
95. Yoda, K.; Imai, K.; Kuroba, K.; Ogawa, K.; Kimura, K.; Motoyui, S. Bending capacity of thin-walled welding H-section beams. *J. Struct. Constr. Eng. (Trans. AIJ)* **1989**, *397*, 60–72. (In Japanese) [CrossRef] [PubMed]
96. Yoshikawa, M.; Suzuki, T.; Ogawa, T.; Kimura, K.; Motoyui, S.; Matsuoka, T. Investigation on estimation of inelastic behavior of H-shaped beam with circular hole. In *Summaries of Technical Papers of Annual Meeting Architectural Institute of Japan*; Japan Society for Finishings Technology: Tokyo, Japan, 1993; pp. 1473–1474. (In Japanese)
97. Ikarashi, K.; Suzuki, T. A study on plastic deformation capacity of H-shaped stiffened beams with web opening. In *Summaries of Technical Papers of Annual Meeting Architectural Institute of Japan*; Japan Society for Finishings Technology: Tokyo, Japan, 2000; pp. 505–506. (In Japanese)
98. *JIS Z 2241*; Metallic Materials-Tensile Testing Method of Test at Room Temperature. Japan Industrial Standards (JIS): Tokyo, Japan, 2011.
99. *EN 1998-1*; Eurocode 8: Design of Structures for Earthquake Resistance—Part 1: General Rules, Seismic Actions and Rules for Buildings. European Committee for Standardization: Brussels, Belgium, 2004.
100. *EN 1998-3*; Eurocode 8: Design of Structures for Earthquake Resistance—Part 3: Assessment and Retrofitting of Buildings. European Committee for Standardization: Brussels, Belgium, 2005.
101. Kadono, A.; Sasaki, M.; Okamoto, K.; Akiyama, H.; Matsui, C.; Inoue, K. Experimental study on the effect of yield ratio on the bending strength increasing ratio and the ductility of steel structures' members. *J. Struct. Eng.* **1994**, *40B*, 673–682. (In Japanese)
102. Suzuki, T.; Ikarashi, K.; Satsukawa, K. Estimate for plastic deformation capacity of steel members with moment gradient reflected material properties. *J. Struct. Constr. Eng. (Trans. AIJ)* **2000**, *537*, 129–134. (In Japanese) [CrossRef]